5th Madrid Turbulence Workshop IOP Publishing
Journal of Physics: Conference Series **2753** (2024) 012010 doi:10.1088/1742-6596/2753/1/012010

The role of nonlinear interactions in the onset of drag increase in flow over riblets

B Viggiano[1], **C J Camobreco**[2], **J Wong**[2], **M Luhar**[3], **R García-Mayoral**[4], **D Chung**[2] **and D Gayme**[5]
[1]Génie Mécanique, Polytechnique Montréal, Montréal, QC H3T 1J4, Canada
[2]Department of Mechanical Engineering, University of Melbourne, Victoria 3010, Australia
[3]Department of Aerospace and Mechanical Engineering, University of Southern California, Los Angeles, CA 90089, USA
[4]Department of Engineering, University of Cambridge, Cambridge CB2 1PZ, UK
[5]Department of Mechanical Engineering, Johns Hopkins University, Baltimore, MD 21218, USA

E-mail: `bianca.viggiano@polymtl.ca`

Abstract. Characterizing the mechanisms that contribute to the onset of drag increase over micro-grooves (riblets) as the spacing increases is critical to design strategies for riblet-based drag reduction. This study decomposes the roughness function to investigate different mechanisms associated with the breakdown of drag reduction as riblet spacing is increased. We obtain the roughness function through direct numerical simulations (DNS) in a minimal channel and restricted nonlinear (RNL) models. Both the traditional RNL decomposition and an augmented RNL (ARNL) model that includes additional nonlinear interactions are employed as computationally tractable, reduced order representations of the flow field. RNL and ARNL results are compared to those of DNS in minimal channels to investigate the role of the different scale-dependent nonlinear interactions contributing to the roughness function. A comparison of the co-spectra arising from the minimal channel DNS with that from RNL and ARNL simulations indicates that general trends are captured by both reduced order models. However, the additional nonlinearity introduced in the ARNL model produces closer correspondence in the observed structural features of the DNS results. In particular, the ARNL better captures the signatures of the dispersive flow and the texture-coherent fluctuations. There is also a noticeable improvement observed in the profiles of the added stress contributions obtained with the ARNL model versus the RNL model.

1. Introduction

Transport efficiency losses in a range of aviation applications have been attributed to skin-friction drag [1, 2, 3]. Mitigation of this drag can be achieved through the inclusion of small-scale spanwise-varying surface elevations known as riblets [4]. If sized correctly, riblet lined surfaces in low Reynolds number flows can reduce skin-friction drag by nearly ∼10% compared to a smooth wall [4, 5, 6]. The potential to exploit this behavior in passive flow control has motivated detailed studies of the effect of riblets both experimentally [5, 6] and numerically [7, 8, 9]. For flows over small riblets, the turbulence remains smooth-wall-like, albeit with a wall-normal displacement [10, 11, 12]. Here small refers to riblets with a square-root of groove area $\ell_g^+ \lesssim 10$ [4], and the '+' superscript denotes scaling by the wall shear stress τ_w and kinematic viscosity of the fluid ν. As the spacing is increased, the riblet-induced drag reduction lessens and eventually an increase in drag is seen in flows over larger riblets. An in-depth understanding of this so-called breakdown of riblet-induced drag reduction is required to robustly deploy riblets.

Efforts to understand and further define the mechanisms underlying the breakdown of riblet-induced drag reduction have focused on contributions to the roughness function. The roughness function $\Delta U^+ \equiv U_S^+ - U_R^+$ quantifies the shift between the mean streamwise velocity profile of the flow over smooth and riblet surfaces, denoted by the subscripts S and R, respectively. García-Mayoral *et al.* (2011) [13] decomposed the change in skin-friction coefficient (related to ΔU^+) into contributions from the slip velocity and the effect of extra Reynolds stresses. Contributions to the roughness function ΔU^+ have also been studied for rough and permeable surfaces [14, 15]. Endrikat *et al.* (2021) [9] recently performed a detailed campaign of numerical simulations for multiple riblet geometries and spacings to assess the contribution of Kelvin–Helmholtz-like (spanwise) rollers to ΔU^+. They also assessed their role in the breakdown of the drag-reduction. Although this role was previously noted in blade riblet geometries [4], the results in [9] showed that spanwise rollers only formed for certain riblet geometries and only accounted for a portion of the drag increase.

In smaller riblets, the effects of extra Reynolds stresses, e.g. as considered in García-Mayoral *et al.* (2011) [13], are negligible. The roughness function is then directly related to the virtual origins of the mean velocity ℓ_U^+ and of the turbulence ℓ_T^+, i.e. $\Delta U^+ = -(\ell_U^+ - \ell_T^+)$ [10, 11], where ℓ_U^+ and ℓ_T^+ are both measured from the riblet crests and defined as positive toward the groove floors. Accurately measuring ΔU^+ and the virtual origins ℓ_U^+ and ℓ_T^+ in a self-consistent manner is more challenging for larger riblets (at sizes when the drag reduction breaks down). First, the turbulence is no longer smooth-wall-like, and the resulting difference in Reynolds shear stresses (between smooth and riblet walls) contributes to the roughness function, i.e. $\Delta U^+ = -(\ell_U^+ - \ell_T^+) + \Delta U^+_{u'v'}$, where, e.g. $\Delta U^+_{u'v'} = \int \left[-\langle u'_S v'_S\rangle^+_{x,z,t} + \langle u'_R v'_R\rangle^+_{x,z,t}\right] \mathrm{d}y^+$. Here, subscripts S or R on velocity fluctuations u' and v' respectively refer to smooth or riblet lined walls, and angled brackets indicate averaging over the directions specified in the subscript. Second, although the uncertainties in ΔU^+ and ℓ_U^+ are relatively small for riblets with sizes $10 \lesssim \ell_g^+ \lesssim 20$, cf. [12], uncertainties in the turbulence origin ℓ_T^+ and Reynolds stress contribution $\Delta U^+_{u'v'}$ become large (given that both are related). While this issue does not prevent measuring an approximate friction velocity that characterizes the shifted but otherwise similar log-layer of the flow above rough walls and canopies (as related to either a zero-plane-displacement or penetration depth [16, 17, 18, 19, 20]), it hampers understanding of the drag-increasing mechanisms.

Measuring ΔU^+ requires both a clearly defined log-layer and a log-layer slope (von Kármán constant) matched with that of a smooth wall. Thus, the thickness of the boundary layer (set by, e.g. the channel height) must be much larger than the height of the roughness sublayer [21]. Outer-layer similarity must also be maintained both in the wake and the log-layer [20]. This condition is typically satisfied when the characteristic lengths of the outer scales are much larger than the characteristic lengths of the roughness. In a numerical setting, the log-layer measured roughness function ΔU^+ can be efficiently obtained by constraining the dimensions of the periodic box and by presuming outer-layer similarity. These minimal log-layer channels have been shown to capture both near-wall and log-layer turbulence over a smooth wall, up to a given critical wall-normal location within the outer-layer similar region [22]. For rough walls, this minimal channel technique was similarly shown to correctly predict the velocity shift ΔU^+ [23] and spectrally truncated turbulent quantities [24], although the technique is unable to predict the bulk velocity directly. Furthermore, one of the drag-increasing contributions to ΔU^+, specifically, that associated with spanwise rollers, is reproduced by minimal channels [25]. While even smaller minimal buffer-layer channels can capture individual coherent structures (e.g. a single streak) [26], these smaller domains do not encompass the logarithmic region required to simultaneously measure ΔU^+ and the mechanisms contributing to it. Thus, contributions to the roughness function ΔU^+ for riblets up to and just beyond drag-breakdown will be assessed herein with minimal log-layer channels.

The fine resolution required for DNS of flows over riblets has also motivated the use of more computationally efficient reduced order flow representations. In particular, the correlation between skin-friction drag [16, 27] and the coherent structures in wall-bounded turbulence motivates a coherent structure based representation, such as the RNL model [28]. This modeling framework has been shown to reproduce salient features of low and moderate Reynolds number wall-bounded turbulence [29, 30, 28], as well as riblets and non-homogeneous rough surfaces [31] at vastly reduced computational expense. This model decomposes the flow into a large scale streamwise constant mean and small-scale perturbations about that mean, and restricts nonlinear interactions to those contributing to the mean flow. This full representation of the cross-plane motions associated with the secondary flows contributing to $\Delta U^+_{u'v'}$, suggests that an RNL model may be well suited to computationally efficient studies of the associated flow mechanisms. We also introduce an augmented RNL (ARNL) model, which permits intermediate scales to interact nonlinearly with the RNL mean flow but maintains order reduction by dynamically constraining inter-scale interactions [32]. The use of the two models enables the evaluation of the role of the additional nonlinearity in the ARNL model in the mechanisms of interest.

In this work, we aim to study the flow mechanisms that are related to the $\Delta U^+_{u'v'}$ contribution to the roughness function (ΔU^+), and thereby characterize the drag increase generated by larger (post-optimal) riblets. However, mechanisms that appear related to the $\Delta U^+_{u'v'}$ contribution may be misinterpreted if the virtual origin for turbulence ℓ_T^+ (or zero-plane-displacement) is incorrectly identified. Thus, our first aim is to assess the sensitivity of $\Delta U^+_{u'v'}$ to ℓ_T^+, and to further investigate whether portions of the $\Delta U^+_{u'v'}$ contribution can be rendered insensitive to ℓ_T^+, through analysis of minimal channel DNS data. Thereafter, our second aim is to use the RNL and ARNL models to assess whether a reduced set of nonlinear interactions can recover $\Delta U^+_{u'v'}$, while similarly assessing their sensitivity to ℓ_T^+ within these reduced order settings.

The remainder of this paper is organized as follows. We first present the mathematical formulation of the reduced order models in Section 2. The setup of the minimal channel DNS, as well as the RNL and ARNL models is described in Section 3. This is followed by a description of the decomposition of the roughness function in Section 4. The resulting stress contributions are investigated in Section 5. Our final conclusions and outlook for this work are provided in Section 6.

2. Restricted nonlinear models

The RNL and ARNL equations are formed by first decomposing the total velocity and pressure fields, respectively $\boldsymbol{u}(x,y,z,t)$ and $\boldsymbol{p}(x,y,z,t)$, into a mean and perturbations about that mean, i.e., $\boldsymbol{u}(x,y,z,t) = \boldsymbol{U}^\star(x,y,z,t) + \boldsymbol{u}^\star(x,y,z,t)$ and $\boldsymbol{p}(x,y,z,t) = \boldsymbol{P}^\star(x,y,z,t) + \boldsymbol{p}^\star(x,y,z,t)$ Here the mean of the (A)RNL velocity and pressure fields are defined through a spatial filter $\boldsymbol{U}^\star(x,y,z,t) = [\boldsymbol{u}(x,y,z,t)]_l$ and $\boldsymbol{P}^\star(x,y,z,t) = [\boldsymbol{p}(x,y,z,t)]_l$ that limits the contributions to a specified set of streamwise Fourier modes $k_x \in \mathcal{L}$. The perturbations about the mean of the velocity and pressure field are respectively denoted $\boldsymbol{u}^\star(x,y,z,t)$ and $\boldsymbol{p}^\star(x,y,z,t)$. These perturbation fields are also restricted using a small-scale spectral filter, denoted as $[\cdot]_s$, which specifies the support of the perturbation dynamics to the set of modes $k_x \in \mathcal{S}$. The RNL and the ARNL dynamics are given by $\nabla \cdot \boldsymbol{U}^\star = \nabla \cdot \boldsymbol{u}^\star = 0$, and the momentum equations,

$$\partial_t \boldsymbol{U}^\star + [\boldsymbol{U}^\star \cdot \nabla \boldsymbol{U}^\star]_l + \nabla \boldsymbol{P}^\star/\rho - \nu \nabla^2 \boldsymbol{U}^\star = -[\boldsymbol{u}^\star \cdot \nabla \boldsymbol{u}^\star]_l, \tag{1a}$$

$$\partial_t \boldsymbol{u}^\star + [\boldsymbol{U}^\star \cdot \nabla \boldsymbol{u}^\star]_s + [\boldsymbol{u}^\star \cdot \nabla \boldsymbol{U}^\star]_s + \nabla \boldsymbol{p}^\star/\rho - \nu \nabla^2 \boldsymbol{u}^\star = 0. \tag{1b}$$

These models restrict the dynamics by omitting nonlinear interactions between perturbations that do not contribute to the large scale modes $k_x \in \mathcal{L}$. In the RNL model, the single large-scale streamwise mode is $k_x = 0$, i.e. $\boldsymbol{U}^{\star}(y, z, t) = \langle \boldsymbol{u} \rangle_x$ where $\langle \cdot \rangle_x$ denotes streamwise averaging. The RNL small scales, $k_x \neq 0 \in \mathcal{S}$, are restricted to modes in the peak range of the outer-layer surrogate dissipation spectra, see e.g. [30] for further details.

In ARNL the set of large-scale modes $\mathcal{L}$ is expanded to include one or more intermediate scales $k_x \neq 0$ that interact non-linearly with the other *large-scale* modes (i.e. $[\boldsymbol{U}^{\star} \cdot \nabla \boldsymbol{U}^{\star}]_l$ in Eq. 1a). In what follows, we denote the large and intermediate $k_x \in \mathcal{L}$ modes in the ARNL model as K_x to differentiate them from the small-scale modes supporting the perturbation dynamics $k_x \in \mathcal{S}$. Similar to the GQL model [33], the additional large-scale modes $K_x \neq 0$, denoted as $K_x^{(n)}$, interact with the small-scale non-zero modes, e.g. $k_x^{(1)}, k_x^{(2)} \in \mathcal{S}$, in a consistent manner, such that for a given single large-scale non-zero mode, $n = 1$, i.e. $K_x^{(1)}$, $k_x^{(2)} = K_x^{(1)} + k_x^{(1)}$, see [32] for further details. As in the RNL model, the ARNL small scales are taken from the peak region of the surrogate dissipation spectrum. We note that this selection of large and small scales modes differs from the GQL modeling approach, where a cutoff defines the respective small and large scales [33].

3. Simulation setup

The direct numerical simulations (DNS) are performed with the solver Cliff, by Cascade Technologies Inc. [34, 35]. The finite-volume node-based solver is second-order accurate, and solves the full Navier–Stokes equations over a body-fitted grid. All DNS employ minimal channels, where the domain size and simulation times are guided by [23, 36]. Minimal channel domain lengths of $L_x^+ \approx 1000$ and spans $L_z^+ \approx 250$ ensure a critical height up to which turbulence remains realistic of $y_c^+ \approx 100$. Simulations times are accordingly increased to ensure the simulation time L_t scaled by the largest realistic eddy (of size y_c) is at least $L_t u_\tau / y_c \approx 300$. The channel half-heights measured from the riblet mean height are set to $\delta^+ = 395$. For further details, see Table 2 or [9, 12]. DNS data for six blade riblet sizes are investigated, two cases from [9] and four from [12]. All blade riblets have a height to spacing ratio of 0.5 and thickness to spacing ratio of 0.2 (Table 1). Three cases correspond to riblets below the optimal groove area [4], and three above. All except the largest case are drag reducing.

A pseudo-spectral, open-source code (LESGO) is used to solve the RNL and ARNL Eqs. (1a) and (1b). The derivatives in the streamwise and spanwise domain are evaluated using Fourier transforms. Central second-order finite-differences are applied for the wall-normal direction. A hyperbolic tangent stretched coordinate system is used to ensure enough grid points near the roughness elements [37]. A Crank–Nicolson scheme is also implemented in the wall-normal domain for time advancement of the diffusive terms. An Adams–Bashforth scheme is applied for the remaining terms. The simplified dynamics associated with the proposed models allow the nonlinear term to be computed as a convolution in Fourier space (k_x, y, z, t) instead of switching to physical space, saving computational costs [38].

The RNL and ARNL simulations are carried out in a half-channel domain with stress-free $(\partial u/\partial y = \partial w/\partial y = 0)$ and zero permeability boundary conditions imposed at the top and bottom of the calculation domain, respectively. Periodic boundary conditions are applied in the streamwise and spanwise directions. No-slip conditions are imposed at the bottom wall. The riblet surface is defined using the immersed boundary method of [39]. In particular, inside the riblets, a force is applied such that the velocity is set to zero for all time steps. Outside of the riblets, the force is set to zero and therefore the velocity is unchanged. The implementation of the immersed boundary method to the RNL and ARNL representations is described in detail in Minnick (2022) [31].

Three blade riblet sizes are considered for the both RNL and ARNL cases, the riblet geometries and simulation parameters for all cases are provided in Table 1. Smooth wall

Table 1. Characteristics of blade geometries considered, where s^+ is the riblet spacing, and the groove area $A_g^+ = \ell_g^{+2}$. DNS cases are minimal channels; those marked with a ‡ superscript are from [9], and those with a † superscript are from [12]. All riblets cross-sections have $h/s = 1/2$ and $b/s = 1/5$.

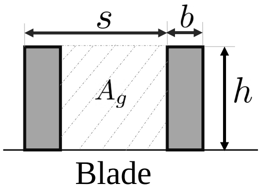

Case	s^+	ℓ_g^+	Case	s^+	ℓ_g^+
BL20$_{\mathrm{RNL}}$	20	12.6	BL08$^\dagger_{\mathrm{DNS}}$	7.8	4.9
BL30$_{\mathrm{RNL}}$	30	19.0	BL12$^\dagger_{\mathrm{DNS}}$	11.9	7.5
BL40$_{\mathrm{RNL}}$	40	25.3	BL16$^\dagger_{\mathrm{DNS}}$	15.6	9.9
BL20$_{\mathrm{ARNL}}$	20	12.6	BL20$^\ddagger_{\mathrm{DNS}}$	20.3	12.8
BL30$_{\mathrm{ARNL}}$	30	19.0	BL25$^\dagger_{\mathrm{DNS}}$	25.0	15.8
BL40$_{\mathrm{ARNL}}$	40	25.3	BL33$^\ddagger_{\mathrm{DNS}}$	33.3	21.1

Table 2. Description of the computational domain and grid resolution for the minimal channel DNS and RNL (including ARNL) simulations, and wavenumbers retained in the RNL and ARNL. L_x^+ and L_z^+ are the streamwise and spanwise domain lengths, respectively, while δ^+ is the domain height measured from the riblet mean height. The resolution in the streamwise, wall-normal and spanwise directions are $\Delta x^+ = u_\tau \Delta x/\nu$, $\Delta y^+ = u_\tau \Delta y/\nu$ (at the riblet tips, and at the channel centreline) and $\Delta z^+ = u_\tau \Delta z/\nu$ (at the riblet tips, for the smallest and largest riblets), respectively.

Case	L_x^+	δ^+	L_z^+	Δx^+	Δy^+	Δz^+
DNS	1002–1027	395	250–264	6	0.30–7.00	0.20–0.83
RNL	-	395	1200	-	0.62–3.41	1
ARNL	-	395	1200	-	0.62–3.41	1

simulations of the RNL and ARNL models with the same resolution and Reynolds number are also performed. Note, the same resolution is employed because this data is used to initialize the RNL and ARNL riblet simulations. For the DNS, the smooth-wall case has similar streamwise and wall-normal resolution, but approximately four times larger spanwise resolution. The details of the computational grids for the DNS and RNL simulations are provided in Table 2. A summary of the streamwise wavenumbers used in the reduced-order models is included in Table 3, where the non-dimensional wavenumber is defined as $k_x\delta = 2\pi\delta/L_x \times (n)$, in which δ is the half-channel height, L_x is the streamwise domain length[1] and n is a non-negative integer. RNL simulations include the streamwise mean, $K_x = 0$ while ARNL cases also include a second large-scale mode, $K_x^{(1)}$, which corresponds to a large-scale wavelength, Λ_x/δ, equal to 0.898, which is the nearest in value to the half-channel height δ. As described above, the small-scale modes supporting the RNL dynamics are associated with wavelengths in the region associated with outer-layer peak of the surrogate dissipation spectrum. While the ARNL small-scales are also constrained to this region, they differ from those in the RNL model to ensure that $k_x^{(2)} = K_x^{(1)} + k_x^{(1)}$.

[1] L_x is used here to define the wavenumber although there is no physical grid used in the reduced order simulations.

Table 3. The wavenumbers and corresponding wavelengths retained in the RNL and ARNL.

Case	$K_x\delta$	$\approx \Lambda_x/\delta$	$k_x\delta$	$\approx \lambda_x^+$
RNL	0	∞	15.5, 16, 16.5	160.1, 155.1, 150.4
ARNL	0, 7	∞, 0.898	12.5, 19.5	198.5, 127.3

4. Texture-coherent contribution to the roughness function

As discussed in Section 1, the roughness function is decomposed as $\Delta U^+ = -(\ell_U^+ - \ell_T^+) + \Delta U^+_{u'v'}$, where, for small riblets, wall turbulence behaves like that over a smooth wall down to the inner viscous sublayer [12], i.e. $\Delta U^+_{u'v'} \approxeq 0$, indicating that the drag increase is only due to a change in virtual origin. For larger riblets, the inner layer changes, where the smooth-wall-like viscous sublayer is replaced by a riblet sublayer such that i.e. $\Delta U^+_{u'v'} \neq 0$. One approach to understand this change is to isolate its texture-coherent contributions from the texture-incoherent contributions [40, 41]. A standard approach to extract the texture-coherent part of $\Delta U^+_{u'v'}$ is to time- and streamwise-average the velocity components, which is generally referred to as the dispersive flow [42]. However, for other non-smooth surfaces, signs of texture-coherence in the remaining fluctuations (instantaneous minus dispersive flow) can still be seen at wavelengths both greater than and less than the roughness spacing, identified as the sidebands of modulation [40, 41, 43]. Thus, a more general class of texture-coherent flows ($\lambda_x^+ \leq \infty$, $\lambda_z^+ \lesssim s^+$), beyond dispersive flows ($\lambda_x^+ \to \infty$, $\lambda_z^+ = s^+, s^+/2, s^+/3, \dots$), will be considered when evaluating texture-coherent contributions to $\Delta U^+_{u'v'}$.

Measuring both ΔU^+ and $\Delta U^+_{u'v'}$ relies on identifying ℓ_T^+. In this work we choose to identify ℓ_T^+ as the wall-normal shift minimizing the sum-squared error in the Reynolds stress profiles, i.e. minimizing $-\langle u'_S v'_S\rangle^+_{x,z,t}(y^+) + \langle u'_R v'_R\rangle^+_{x,z,t}(y_R^+ = y^+ - \ell_T^+)$ at matched y^+ in the vicinity of the maximum-Reynolds-stress gradient. Herein, this range is chosen as $4 \lesssim y^+ \lesssim 6$ [12]. The reference riblet wall-normal coordinate y_R^+ is zero at the riblet crests. This fitting method is only appropriate when the flow is smooth-wall-like (for small riblets), and does not guarantee sensible values of ℓ_T^+ for larger riblets. For small riblets, this method also agrees well with virtual origins defined by profiles of the root-mean-square of the velocity fluctuations [44].

With a turbulence origin identified, this leaves the issue of evaluating the contribution from the difference in the Reynolds shear stress,

$$\Delta U^+_{u'v'} = -\int_{\ell_T^+}^{y_m^+} \langle u'_S v'_S\rangle^+_{x,z,t}(y^+)\,\mathrm{d}y^+ + \int_{\ell_T^+}^{y_m^+} \langle u'_R v'_R\rangle^+_{x,z,t}(y_R^+ = y^+ - \ell_T^+)\,\mathrm{d}y^+, \tag{2}$$

where $y^+ = 0$ is at the smooth wall and $y^+ = y_m^+$ is a wall-normal height within the log-layer, above the riblet sublayer [12]. With flow changes occurring only in the riblet sublayer, i.e. with outer-layer similarity, the difference in Reynolds stress beyond the upper integration limit is zero at matched friction Reynolds number $\delta_S^+ = \delta_R'^+$ ($\delta_R'^+$ is the channel height measured from $y_R^+ = -\ell_T^+$), or is nearly zero with sufficiently thick log layers even if the outer flow is mismatched. Eq. (2) depends on ℓ_T^+ in three ways. First, as the wall-normal coordinates of the Reynolds stress profiles are not matched, but differ by ℓ_T^+. If ℓ_T^+ is uncertain, this can translate to leading order changes in $\Delta U^+_{u'v'}$ for larger riblets. Second, through the lower integration bound, which for riblets starts at the crests ($y_R^+ = 0$), and for the smooth wall starts at ℓ_T^+ above the wall. This is less of an issue than matching wall-normal coordinates, as the smooth-wall Reynolds stresses are small near the wall. Third, through the friction velocity u_τ that defines the wall units for the riblets (although the uncertainty in ℓ_T^+ does not greatly alter u_τ). Overall, these uncertainties present a challenge to interpreting the drag-increasing mechanisms that set the minimum of ΔU^+ and hence the optimal riblet size. This motivates further subdividing $\Delta U^+_{u'v'}$ into contributions from coherent flow structures [9, 13, 42], e.g. from typical secondary (dispersive) flows both above and within the riblets grooves, or from spanwise-coherent rollers above the crests. Assessing the sensitivity of some of these contributions to $\Delta U^+_{u'v'}$ is the first aim of analysing the DNS data.

The first issue is to separate out the dispersive stress contributions due to secondary flows. Defining ΔU^+ based on the mean momentum balance $\partial_y U^+ - \langle u'v' \rangle^+_{x,z,t} = 1 - y/\delta'_R$ [12] above the riblet tips requires, for consistency, that fluctuations are defined by

$$u(x, y, z, t) = \langle u \rangle_{x,z,t}(y) + u'(x, y, z, t), \tag{3}$$

and similarly for v and w. Herein, $u(x, y, z, t)$ is the instantaneous velocity, $\langle u \rangle_{x,z,t}(y)$ is the horizontal plane- and time-averaged velocity, henceforth referred to as the spanwise mean flow, and $u'(x, y, z, t)$ is the fluctuation about this spanwise mean (denoted by $'$). To then separate out the dispersive contribution $\tilde{u}$, a fluctuation about the riblet-average u'' is defined, and u' re-expressed as

$$u'(x, y, z, t) = \tilde{u}(y, z) + u''(x, y, z, t). \tag{4}$$

where $\tilde{u}(y, z) = \langle u \rangle_{x,r,t}(y, z) - \langle u \rangle_{x,z,t}(y)$, following the notation of e.g. [9, 40, 41]. Substituting Eq. (4) into Eq. (3) recovers $u(x, y, z, t) = \langle u \rangle_{x,r,t}(y, z) + u''(x, y, z, t)$, highlighting that u'' represents a fluctuation about the riblet-averaged flow $\langle u \rangle_{x,r,t}$ (the flow within each riblet groove, averaged across all the riblet periods, i.e. averaging across s^+-width segments of the domain). From the decomposition in Eq. (4), the product of fluctuations about the spanwise mean can be re-expressed as

$$\langle u'v' \rangle_{x,z,t} = \langle [\tilde{u} + u''][\tilde{v} + v''] \rangle_{x,z,t}, = \langle u''v'' \rangle_{x,z,t} + \langle \tilde{u}\tilde{v} \rangle_{x,z,t}. \tag{5}$$

Thus, the dispersive contribution $\Delta U^+_D = \int_{\ell^+_T}^{y^+_m} \langle \tilde{u}_R \tilde{v}_R \rangle^+_{x,z,t}(y^+_R = y^+ - \ell^+_T)\,\mathrm{d}y^+$ has been identified, where $\Delta U^+_{u'v'} = \Delta U^+_D + \Delta U^+_{u''v''}$. Note that ΔU^+_D is almost unaffected by ambiguity in ℓ^+_T, apart from the change in friction velocity u_τ (the lower limit of the integral is always at the fixed riblet crest, and there is no dispersive smooth-wall equivalent to cancel with).

The preceding discussion to obtain ΔU^+_D indicates that contributions to $\Delta U^+_{u'v'}$ that do not have smooth-wall counterparts, such as those that are coherent with the texture, are resilient to ambiguity in ℓ^+_T. However, the dispersive contributions alone do not constitute all of the texture-coherent contributions. This is because amplitude modulation of the s^+-periodic dispersive flow by the overlying near-wall turbulence (e.g. quasi-streamwise vortices centered around $\lambda^+_z \approx 50$ [45]) gives rise to spectral content at wavelengths above and below s^+ (and also at wavelengths above and below the harmonics $s^+/2, s^+/3, \dots$) [40, 41]. These λ^+_z-sidebands that flank s^+ are visible in Figure 1(a), at $\lambda^+_x \approx 150$ especially, and in spectra of flow over other textures [46, 47]. Provided sufficient scale separation exists between the texture s^+ and the near-wall turbulence, a simple approach is to deem all Reynolds stress contributions with spanwise wavelengths $\lambda^+_z \lesssim 1.25s^+$ texture coherent ($\Delta U^+_{TCu'v'}$). As illustrated in Figure 1(a), this cut-off includes the modulations sidebands as well as the dispersive flow at $\lambda^+_x \to \infty$. For riblets at larger spanwise spacings s^+ for which scale separation is not sufficient, this texture-coherent cut-off includes near-wall turbulence which may remain texture-incoherent. To minimize this issue, the smooth-wall Reynolds stresses are integrated below the same $\lambda^+_z \lesssim 1.25s^+$ cut-off for each riblet, i.e. $\Delta U^+_{TCu'v'} = \int_{\ell^+_T}^{y^+_m} -\langle u'_S v'_S \rangle^+_{x,z,t}|_{\lambda^+_z \lesssim 1.25s^+}(y^+)\mathrm{d}y^+ + \int_{\ell^+_T}^{y^+_m} \langle u'_R v'_R \rangle^+_{x,z,t}|_{\lambda^+_z \lesssim 1.25s^+}(y^+_R = y^+ - \ell^+_T)\mathrm{d}y^+$.

The isolation of both dispersive and more general texture-coherent contributions in the analysis of the RNL and ARNL models will further highlight the capabilities and limitations (*a*) DNS

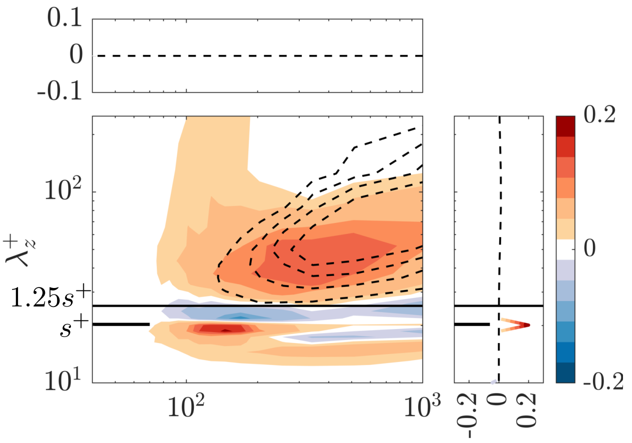

(*b*) RNL (*c*) ARNL

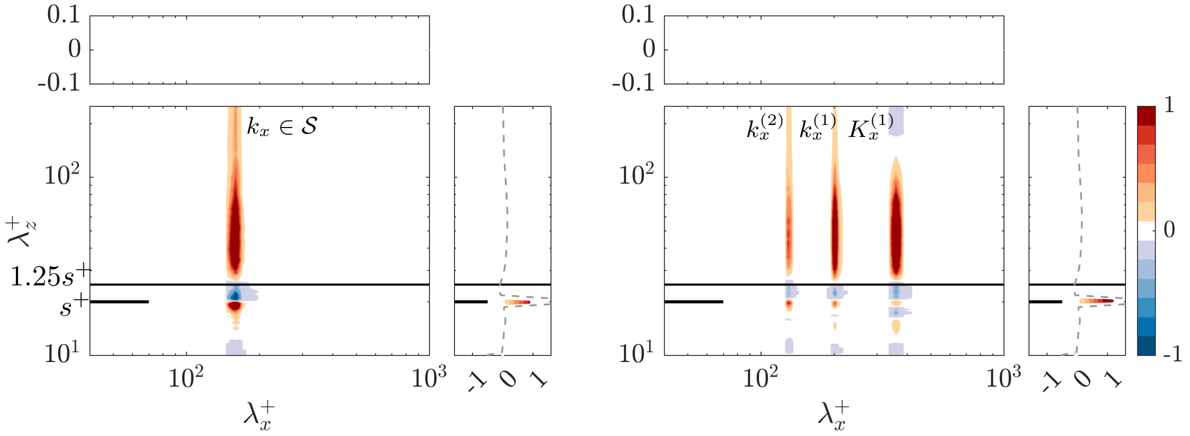

Figure 1. Premultiplied Reynolds stress co-spectra $\langle u'v' \rangle^+$ for $\ell_g^+ \approx 12.8$ blade riblets at $y_R^+ \approx 1$ (colored contours), normalized by the integral of the Reynolds stresses at this y_R^+. (*a*) Minimal log-layer channel DNS. (*b*) RNL model. (*c*) ARNL model. For the DNS in (*a*), the smooth wall spectra are included in dashed black contours at $y^+ \approx 1 + \ell_T^+$ (extrapolated model ℓ_T^+), plotting every second level. For the RNL and ARNL in (*b*, *c*), the dashed gray curves are the sum of the DNS Fourier coefficients for all modes with $\lambda_x^+ \gtrsim 314$. For clarity, premultiplied Reynolds stresses with absolute values < 0.01 have been removed. The RNL and ARNL model show spectra until $\lambda_z^+ = 250$ for consistency with the truncated minimal channel DNS.

of these reduced order models. The RNL model only allows nonlinear interactions between streamwise Fourier modes that contribute to the mean flow, $K_x^{(0)}$, while the ARNL model includes additional triadic contributions to the non-zero 'large-scale' mode, $K_x^{(1)}$. The comparison of $\Delta U^+_{u'v'}$ and $\Delta U^+_{u''v''}$ from both RNL and ARNL thus allows investigation of whether these additional nonlinear improve fidelity of the representation of dispersive stresses due to the riblets.

5. Discussion

5.1. Reynolds stress co-spectra

Figure 1(a) shows the premultiplied Reynolds stress co-spectra computed from the minimal channel DNS. Included in this figure is the $1.25s^+$ demarcation of spectral space for just post-optimal riblets ($\ell_g^+ \approx 12.8$, $s^+ \approx 20.3$), where all Reynolds stress contributions in the region $\lambda_z^+ \lesssim 1.25s^+ \approx 25$ are approximated as texture coherent (i.e. are included in $\Delta U^+_{TCu'v'}$), which includes the dispersive contribution ΔU_D^+. Note that the smooth wall contours (dashed lines) remain above the $1.25s^+$ cut-off for this s^+, and so provide almost no cancellation with the texture-coherent Reynolds stresses in the vicinity of s^+, thus improving the robustness of the $\Delta U^+_{TCu'v'}$ measurement. The sidebar of Figure 1(a) also highlights the signature of dispersive flows in the $\lambda_x^+ \to \infty$ and $\lambda_z^+ \leq s^+$ modes, which increase drag via $\Delta U^+_{TCu'v'}$ and are less sensitive to differences in ℓ_T^+. This dispersive signature at $\lambda_x^+ \to \infty$ and $\lambda_z^+ \leq s^+$ vanishes when instead defining fluctuations about the riblet average, and so is not measured in $\Delta U^+_{TCu''v''}$, recalling Eq. (5), and as considered in Section 5.2.

The co-spectra of the RNL model and the ARNL model output are provided in Figures 1(b, c) for a similar riblet spacing of $s^+ \approx 20$. Although the DNS, RNL, and ARNL spectra integrate to similar Reynolds stress values, the RNL and ARNL spectral densities display higher magnitudes because the non-zero streamwise wavenumber support of the dynamics comprises narrow spectral regions. Both models are able to capture the signature of the dispersive stresses in the $K_x = 0$ mode, as observed in the sidebar of Figure 1(b,c), although the DNS estimate here, which includes $\lambda_x^+ \gtrsim 314$, exceeds that of the RNL. Texture-coherent flow signatures in the $\langle u'v' \rangle$ co-spectra are also observed near $s^+ \approx 20$ in the limited RNL and ARNL modes, Figures 1(b,c). For the texture-coherent flows in particular, the signs of the Reynolds stress signatures from RNL and ARNL models match those of the DNS (negative just above s^+, positive just below s^+), for all resolved streamwise scales. These sidebands, cf. [40], suggest that the restricted modes and nonlinear interactions included in both RNL and ARNL are sufficient to capture the modulation effect. We note the inclusion of the intermediate mode at $K_x\delta = 7$ in the ARNL model enables closer comparison with the DNS. The improvement of the ARNL model is evidenced by the redistribution of $\langle u'v' \rangle$ across the three λ_x^+ values, as is similarly observed in the DNS.

5.2. Drag breakdown

Before investigating the decomposition of ΔU^+, the sensitivity of ΔU^+ to the selection of the virtual origin is evaluated by comparing results obtained using an ℓ_T^+ value based on the fitting described in Section 4 and one computed using an extrapolated model (to be described later). The analysis focuses on riblet spacings associated with drag-reduction breakdown. The first approach, as described in Section 4, measures ℓ_T^+ by minimizing the difference between the smooth and riblet DNS Reynolds stress profiles, with the resulting ΔU^+ values depicted in Figure 2(a), ■ markers. The second approach instead employs an extrapolated value for ℓ_T^+, extrapolated from smaller riblet sizes, and is shown in Figure 2(b), ■ markers. As an example, considering the results at $\ell_g^+ \approx 21$, ΔU^+ dropped from ≈ 0.7 to ≈ 0.3 when switching from the first-approach $\ell_T^+ \approx 5.7$, Figure 2(a), to the second-approach $\ell_T^+ \approx 2.4$, Figure 2(b). Note that the mean velocity profiles are normalized by the u_τ consistent with the chosen ℓ_T^+, before the mean flow offsets ΔU^+ are measured above the roughness sublayer ($50 \lesssim y^+ \lesssim 100$ for the minimal channel DNS). The friction velocities consistent with the fitted and extrapolated model ℓ_T^+ differed by $\approx 0.4\%$, where a 1% change in u_τ typically leads to an $\approx 10\%$ change in ΔU^+. Thus, addressing ambiguity in ℓ_T^+ is more important than addressing ambiguity in u_τ, with the ambiguous ℓ_T^+ having noticeably impacted ΔU^+ for post-optimal riblets, at least for $10 \lesssim \ell_g^+ \lesssim 20$. For reference, the extrapolated model ℓ_T^+ values are extrapolated from the virtual origins obtained for small ($\ell_g^+ \lesssim 10$) riblets [12]. These assume $\ell_T^+ \approx h_\perp^+ + m_T {\ell_g^+}^2$, where $h_\perp^+$

is the riblet perpendicular protrusion height [6, 48], and where m_T is the gradient of the ℓ_T/ℓ_g versus ℓ_g^+ curve for small riblets. The viscous model [12] employed to predict this ℓ_T/ℓ_g versus ℓ_g^+ curve maintains good agreement with DNS-fitted ℓ_T^+ values for small riblets ($\ell_g^+ \lesssim 10$), and the DNS-fitted ℓ_T^+ values for small riblets could equally have been extrapolated directly.

Even having shown that the ΔU^+ measurements are impacted by ambiguity in ℓ_T^+, the overall aim remains unchanged: to assess the texture-coherent contributions $\Delta U^+_{TCu'v'}$ which may remain resilient to ambiguity in ℓ_T^+. Thus, the drag breakdown, excluding the highly sensitive texture-incoherent contributions ($\Delta U^+_{TIu'v'}$), becomes $\Delta U^+ \approx -(\ell_U^+ - \ell_T^+) + \Delta U^+_{TCu'v'}$. As shown in Figure 2($a$), the smooth-wall-like and texture coherent-contributions $-(\ell_U^+ - \ell_T^+) + \Delta U^+_{TCu'v'}$ do not recover ΔU^+ with the fitted ℓ_T^+. Thus, a large texture-incoherent Reynolds stress contribution $\Delta U^+_{TIu'v'}$, which is drag reducing, would be required for the mean-momentum budget to balance (note that due to sensitivity to ℓ_T^+, $\Delta U^+_{TIu'v'}$ is not computed separately). However, when using the extrapolated model ℓ_T^+, as shown in Figure 2(b), the texture-incoherent contribution $\Delta U^+_{TIu'v'}$ is now drag increasing, although much smaller in magnitude. Thus, without a method to unambiguously identify ℓ_T^+, no firm statements can be made about some of the drag-reducing or -increasing mechanisms leading to the eventual drag breakdown of riblets. While the Reynolds stress contribution $\Delta U^+_{u'v'}$ has typically been thought to be drag increasing, e.g. [6, 13, 42, 24], explanations have also been put forward that larger riblets may pin the quasi-streamwise vortices, stabilizing the near-wall streaks and thereby reducing drag [49, 50]. For these larger riblets, whether it is appropriate to define ℓ_T^+ is also debatable when the flow is no longer smooth-wall-like. However, ℓ_T^+ should still be retained to allow for a gradual continuation into the larger-riblet regime in which outer-layer similar turbulence presumably remains, otherwise its complete exclusion from the $\Delta U^+ = -(\ell_U^+ - \ell_T^+) + \Delta U^+_{u'v'}$ decomposition could artificially inflate the relevance and meaning of $\Delta U^+_{u'v'}$.

The magnitudes of the dispersive and texture-coherent contributions for the DNS are now considered, as is their resilience to ambiguity in ℓ_T^+. The dispersive contributions are represented by the difference between the — and — curves in Figures 2(a, b), this difference only affected by u_τ and not by ℓ_T^+ directly. Similarly, the texture-coherent contributions are represented by the difference between the — and — curves in Figures 2(a, b). The texture-coherent contributions are weakly sensitive to ℓ_T^+ due to a small cancellation with some smooth wall Reynolds stress contributions below $\lambda_z \lesssim 1.25s^+$, but overall the differences between the — and — curves when comparing Figures 2(a, b) are minimal. When taking the extrapolated model ℓ_T^+ values as a more sensible extrapolation for larger riblets, the total smooth-wall-like and texture-coherent contributions in Figure 2(b), i.e. $-(\ell_U^+ - \ell_T^+) + \Delta U^+_{TCu'v'}$ (— curve), come closer to recovering the measured ΔU^+ (— curve). Thus, texture incoherent contributions may not be greatly important for just post-optimal riblets, so long as the correct virtual origin (which may be close to the model extrapolation) can be identified.

Figures 2(c, d) show the same results as in Figures 2(a, b) based on the RNL simulations, alongside a comparison to the mean flow offsets measured from DNS (■). Again, the drag decomposition is performed based on fitted ℓ_T^+ values as well as the extrapolated model ℓ_T^+ values, as described above for the DNS in the respective discussion of Figures 2(a, b). Here, there are similar trends are to those observed in the DNS decomposition of the roughness function based on the fitted ℓ_T^+ value, presented in Figure 2(a). More specifically, good agreement is observed for all methods for the smallest riblets investigated, and, as the spacing increases, the measured ΔU^+ is not fully recovered. However, the magnitude of the decomposition is underrepresented by the RNL model. Given this method of calculating the turbulence virtual origin provides an underestimation of the added stresses and in turn, the curves actually follow closely the offset for the fitted ℓ_T^+ values. This behavior is not equivalent to that observed for the DNS, nor is the over estimation of stresses based on the extrapolated model ℓ_T^+ values. Although the DNS data also

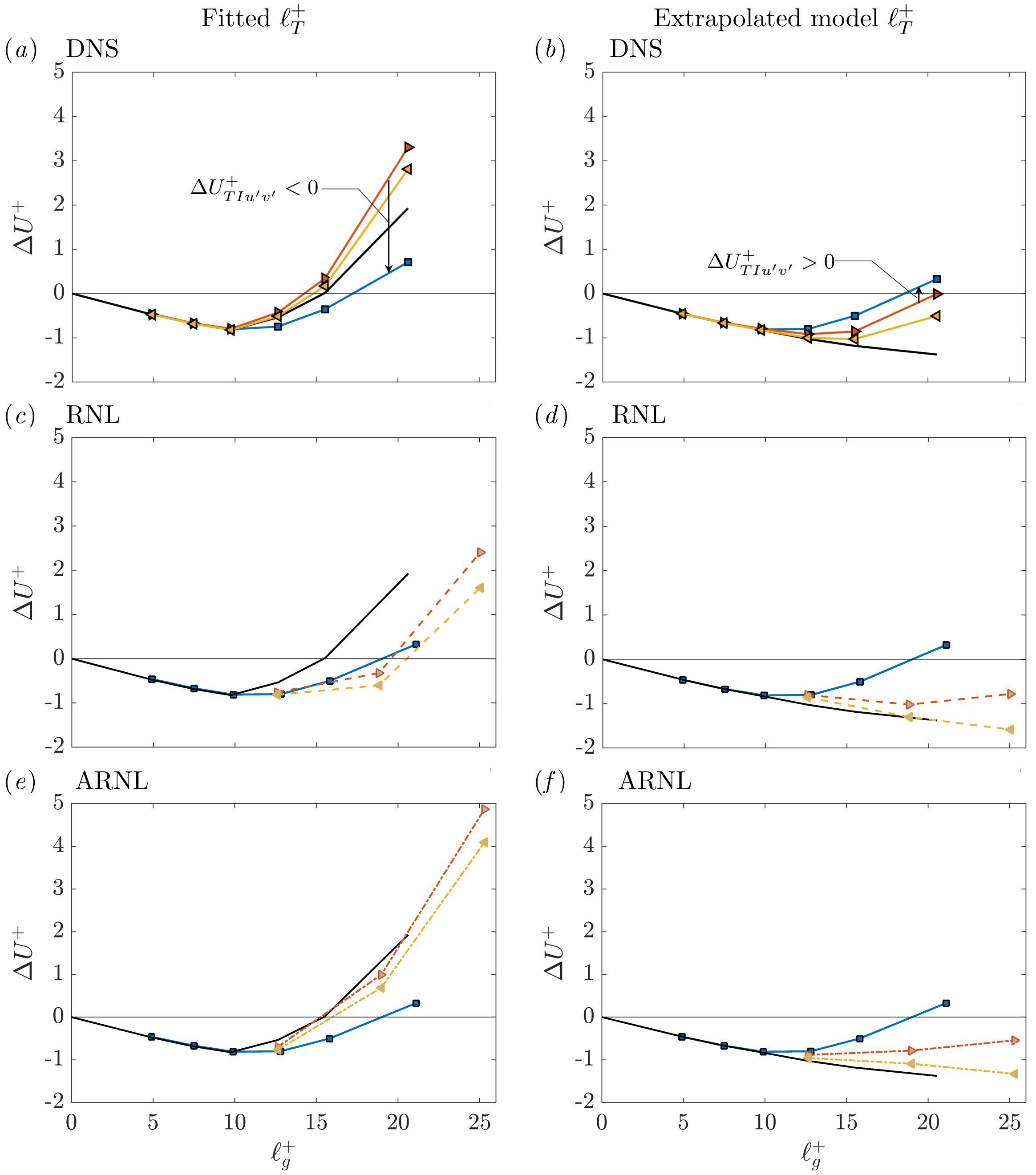

Figure 2. (a) Comparing the DNS-measured ΔU^+ to decompositions of ΔU^+ based on fitted virtual origins ℓ_T^+. For $\ell_g^+ \lesssim 10$, $\Delta U^+ \approxeq -(\ell_U^+ - \ell_T^+)$. For larger ℓ_g^+, the non-zero $\Delta U^+_{TIu'v'}$ is sensitive to ℓ_T^+. ■: ΔU^+ (log-layer measurement), ——: $(-\ell_U^+ - \ell_T^+)$, ▶: $-(\ell_U^+ - \ell_T^+) + \Delta U^+_{TCu'v'}$, ◀ : $-(\ell_U^+ - \ell_T^+) + \Delta U^+_{TCu''v''}$. ($b$) As in ($a$), except with extrapolated model ℓ_T^+ values [12]. For the decomposition to balance, $\Delta U^+_{TIu'v'}$ would now be drag increasing, rather than drag reducing. (c) The same decompositions as for the DNS except with the RNL results, with the RNL-fitted ℓ_T^+, compared to the DNS-measured ΔU^+. (d) As in (c), except with the extrapolated model ℓ_T^+ values [12]. (e) The same decompositions as for the DNS except with the ARNL results, with the ARNL-fitted ℓ_T^+, compared to the DNS-measured ΔU^+. (f) As in (e), except with the extrapolated model ℓ_T^+ values. RNL and ARNL curves are denoted with dashed and dashed-dotted lines, respectively. For the reduced order models the markers are specified as ■: ΔU^+ (log-layer measurement - DNS), ▷: $-(\ell_U^+ - \ell_T^+) + \Delta U^+_{TCu'v'}$, ◁ : $-(\ell_U^+ - \ell_T^+) + \Delta U^+_{TCu''v''}$.

indicates that $\Delta U^+_{TIu'v'}$ may be drag increasing for the fitted ℓ_T^+ case, the RNL overestimates its effect. These discrepancies could in part be due to the inability of the RNL model to capture all of the nonlinearities of the flow over the larger riblets, indicating that the missing nonlinearity may play an important role the mechanisms associated with the texture incoherent contribution $\Delta U^+_{TIu'v'}$.

We next investigate whether capturing additional nonlinearity improves these estimates by introducing the specific intermediate modes to interact nonlinearly in the ARNL model described in Section 2. Figures 2(e, f) present the same decomposition of the roughness function ΔU^+ for the fitted ℓ_T^+ and extrapolated model ℓ_T^+ values based on ARNL simulations, along with the DNS measured mean flow offsets (🟦). Figure 2(e) shows curves which are very similar to those observed in the DNS decomposition of the roughness function. Here, good agreement is not only observed in the just post-optimal spacings but also during the onset of the drag increase regime. However, the curves over-estimate the drag increase and $\Delta U^+_{TIu'v'} < 0$. The extrapolated model ℓ_T^+ curves, Figure 2(f), present over-estimations of $\Delta U^+_{TIu'v'}$, similar to those present for the RNL model but less extreme in comparison to the DNS curves. As the ARNL framework allows additional nonlinearity to be added it would be of interest to probe whether one or more additional intermediate scales further improves the model fidelity.

6. Conclusions and Outlook

The onset of drag increase in turbulent flow over riblets is investigated through the decomposition of the roughness function. The nonlinear interactions are highlighted through comparisons of the decomposed stresses resulting from minimal channel log-layer DNS, the RNL and ARNL models. From analysis of the DNS dataset, there are three conclusions. First, for riblets of sizes $10 \lesssim \ell_g^+ \lesssim 20$, sensitivity in the measured ΔU^+ due to ambiguity in the turbulence origin ℓ_T^+ is non-trivial (for larger ℓ_g^+, the magnitude of ΔU^+ is much larger, and this is less of an issue). Second, for riblets of sizes $\ell_g^+ \gtrsim 10$, ambiguity in ℓ_T^+ can alter whether Reynolds stress contributions appear as drag reducing or as drag increasing. Finally, decomposing the Reynolds stress contributions by extracting the texture-coherent parts can alleviate sensitivity issues, with $\Delta U^+_{TCu'v'}$ even coming close to accounting for all of $\Delta U^+_{u'v'}$ for post-optimal riblets for one sensibly identified set of ℓ_T^+ values.

The 2D co-spectra of the spanwise- and riblet-averaged stress from the minimal channel DNS data and both the ARNL and RNL models present similar trends. The dispersive signature is observed in all the model outputs. Again better agreement is observed between the DNS and the ARNL model versus the RNL model co-spectra, although the differences are less pronounced than those observed in the roughness function decomposition. All reduced order models show similar structures to those of the DNS.

The stress contribution decomposition is not well captured in the RNL model but with the addition of the intermediate scale of the ARNL reduced order model, similar trends to those observed in the DNS are recovered. It is of note that the ARNL model uses the same number of non-zero wavenumbers as the RNL model, but captures the dynamics observed in the DNS with higher accuracy due to its construction and the allowed nonlinear interactions. Therefore this additional fidelity does not pose a significant increase in computational cost.

This project will continue to assess the capabilities of the reduced order models in capturing the nonlinearities observed in the DNS. One method to better understand the abilities of the RNL and ARNL models is to isolate the contributions of individual streamwise modes for the two models to better understand their specific contributions to the spectra and to the added stresses. The results will help to understand how the intermediate mode in the ARNL model interacts with the small-scale modes (and how that compares to the RNL model), and in turn, its role in the representation of the dynamics above the riblets.

Acknowledgements

This work was partially supported by the European Research Council (Caust grant ERC-AdG-101018287) and the US National Science Foundation (grant no. 1652244). Simulations employed the Advanced Research Computing at Hopkins (ARCH) core facility (rockfish.jhu.edu), which is supported by the National Science Foundation (OAC 1920103). C. C., J. W. and D. C. gratefully acknowledge the support of the Air Force Office of Scientific Research under award number FA2386-21-1-4018 (program managers: D. J. Newell and R. W. Carr, AOARD). We also thank D. R. Smith (EOARD) and G. L. Abate (AFOSR).

References

[1] Bushnell D 1983 Turbulent drag reduction for external flows *21st Aerospace Sciences Meeting* p 227
[2] Viswanath P R 2002 *Prog. Aerosp. Sci.* **38** 571–600
[3] Spalart P R and McLean J D 2011 *Phil. Trans. R. Soc. A* **369** 1556–1569
[4] García-Mayoral R and Jiménez J 2011 *Phil. Trans. R. Soc. A* **369** 1412–1427
[5] Walsh M 1982 Turbulent boundary layer drag reduction using riblets *20th Aerospace Sciences Meeting* p 169
[6] Bechert D W, Bruse M, Hage W, Van Der Hoeven J G T and Hoppe G 1997 *J. Fluid Mech.* **338** 59–87
[7] Choi H, Moin P and Kim J 1993 *J. Fluid Mech.* **255** 503–539
[8] Garcia-Mayoral R and Jiménez J 2012 *Phys. Fluids* **24** 105101
[9] Endrikat S, Modesti D, García-Mayoral R, Hutchins N and Chung D 2021 *J. Fluid Mech.* **913** A37
[10] Luchini P 1996 Reducing the turbulent skin friction *Computational methods in applied sciences '96 (Paris, 9-13 September 1996)* ed Désidéri J A, Hirsch C, Le Tallec P, Oñate E, Pandolfi M, Périaux J and Stein E (John Wiley, Chichester United Kingdom) pp 465–470
[11] Ibrahim J I, Gómez-de-Segura G, Chung D and García-Mayoral R 2021 *J. Fluid Mech.* **915** A56
[12] Wong J, Camobreco C J, García-Mayoral R, Hutchins N and Chung D 2024 *J. Fluid Mech.* **978** A18
[13] García-Mayoral R and Jiménez J 2011 *J. Fluid Mech.* **678** 317–347
[14] MacDonald M, Chan L, Chung D, Hutchins N and Ooi A 2016 *J. Fluid Mech.* **804** 130–161
[15] Gómez-de-Segura G and García-Mayoral R 2019 *J. Fluid Mech.* **875** 124–172
[16] Raupach M R, Antonia R A and Rajagopalan S 1991 *Appl. Mech. Rev.* **44** 1–25
[17] Perry A E, Schofield W H and Joubert P N 1969 *J. Fluid Mech.* **37** 383–413
[18] Nikora V I, Koll K, Mclean S R, Ditrich A and Aberle J 2002 Zero-plane displacement for rough-bed open-channel flows *Fluvial Hydraulics River Flow* pp 83–92
[19] Luhar M, Rominger J and Nepf H 2008 *Environ. Fluid Mech.* **8** 423–439
[20] Chen Z and García-Mayoral R 2023 *J. Fluid Mech.* **973** A31
[21] Jiménez J 2004 *Annu. Rev. Fluid Mech.* **36** 173–196
[22] Flores O and Jiménez J 2010 *Phys. Fluids* **22** 071704
[23] Chung D, Chan L, MacDonald M, Hutchins N and Ooi A 2015 *J. Fluid Mech.* **773** 418–431
[24] Endrikat S, Newton R, Modesti D, García-Mayoral R, Hutchins N and Chung D 2022 *J. Fluid Mech.* **952** A27
[25] Endrikat S, Modesti D, MacDonald M, García-Mayoral R, Hutchins N and Chung D 2021 *Flow Turbul. Combust.* **107** 1–29
[26] Jiménez J and Moin P 1991 *J. Fluid Mech.* **225** 213–240
[27] Castro I P 2007 *J. Fluid Mech.* **585** 469–485
[28] Gayme D F and Minnick B A 2019 *Phys. Rev. Fluids* **4** 110505
[29] Bretheim J U, Meneveau C and Gayme D F 2015 *Phys. Fluids* **27** 011702
[30] Minnick B A and Gayme D F 2019 Characterizing energy transfer in restricted nonlinear wall-bounded turbulence *International Symposium on Turbulence and Shear Flow Phenomena (TSFP-11)*
[31] Minnick B A 2022 *A Restricted Nonlinear Approach to Momentum and Scalar Mixing in Wall-Turbulence* Ph.D. thesis Johns Hopkins University
[32] Minnick B A, Viggiano B and Gayme D F 2023 Augmented Restricted Nonlinear (ARNL) Model for High Reynolds Number Wall-Turbulence *Progress in Turbulence X: Proceedings of the iTi Conference on Turbulence 2023* (Springer)
[33] Marston J B, Chini G P and Tobias S M 2016 *Phys. Rev. Lett.* **116** 214501
[34] Ham F, Mattsson K and Iaccarino G 2006 Accurate and stable finite volume operators for unstructured flow solvers *CTR Annu. Res. Briefs* (Center for Turbulence Research) pp 243–261
[35] Ham F, Mattsson K, Iaccarino G and Moin P 2007 Towards time-stable and accurate LES on unstructured grids *Complex Effects in Large Eddy Simulations. Lecture Notes in Computational Science and Engineering, vol. 56* ed Kassinos S C, Langer C A, Iaccarino G and Moin P (Springer, Berin Heidelberg) pp 235–249

[36] MacDonald M, Chung D, Hutchins N, Chan L, Ooi A and García-Mayoral R 2017 *J. Fluid Mech.* **816** 5—42
[37] Jelly T O, Jung S Y and Zaki T A 2014 *Phys. Fluids* **26** 095102
[38] Bretheim J U, Meneveau C and Gayme D F 2018 *J. Turbul.* **19** 141–166
[39] Peskin C S 2002 *Acta Numer.* **11** 479–517
[40] Abderrahaman-Elena N, Fairhall C T and García-Mayoral R 2019 *J. Fluid Mech.* **865** 1042–1071
[41] Xie W 2022 *The Effect of Texture Granularity on Turbulence* Ph.D. thesis University of Cambridge
[42] Modesti D, Endrikat S, Hutchins N and Chung D 2021 *J. Fluid Mech.* **917** A55
[43] Fairhall C T, Abderrahaman-Elena N and García-Mayoral R 2019 *J. Fluid Mech.* **861** 88–118
[44] Gómez-de-Segura G and García-Mayoral R 2020 *Int. J. Heat Fluid Flow* **86** 108675
[45] Jiménez J, Del Álamo J C and Flores O 2004 *J. Fluid Mech.* **505** 179–199
[46] Fairhall C T and García-Mayoral R 2018 *Flow Turbul. Combust.* **100** 961–978
[47] Sharma A and García-Mayoral R 2020 *J. Fluid Mech.* **888** A2
[48] Luchini P, Manzo F and Pozzi A 1991 *J. Fluid Mech.* **228** 87–109
[49] Goldstein D, Handler R and Sirovich L 1995 *J. Fluid Mech.* **302** 333–376
[50] Goldstein D B and Tuan T C 1998 *J. Fluid Mech.* **363** 115–151